remote sensing

MDPI

Article

Signal Photon Extraction and Classification for ICESat-2 Photon-Counting Lidar in Coastal Areas

Yue Song [1], Yue Ma [1], Zhibiao Zhou [1], Jian Yang [1] and Song Li [1,2,*]

[1] School of Electronic Information, Wuhan University, Wuhan 430072, China; 2022182120079@whu.edu.cn (Y.S.); mayue_eis@whu.edu.cn (Y.M.); zhouzhizbiao@whu.edu.cn (Z.Z.); jianyang@whu.edu.cn (J.Y.)
[2] Wuhan Institute of Quantum Technology, Wuhan 430206, China
* Correspondence: ls@whu.edu.cn

Abstract: The highly accurate data of topography and bathymetry are fundamental to ecological studies and policy decisions for coastal zones. Currently, the automatic extraction and classification of signal photons in coastal zones is a challenging problem, especially the surface type classification without auxiliary data. The lack of classification information limits large-scale bathymetric applications of ICESat-2 (Ice, Cloud, and Land Elevation Satellite-2). In this study, we propose a photon extraction–classification method to process geolocated photons in coastal areas from the ICESat-2 ATL03 product. The basic idea is to extract the signal photons using an adaptive photon clustering algorithm, and the extracted signal photons are classified based on the accumulated histogram and triangular grid. We also generate the bottom profile using the weighted interpolation. In four typical coastal areas (artificial coast, natural coast, island, and reefs), the extraction accuracy of a signal photons exceeds 0.90, and the Kappa coefficients of four surface types exceed 0.75. This method independently extracts and classifies signal photons without relying on auxiliary data, which can greatly improve the efficiency of obtaining bathymetric points in all kinds of coastal areas and provide technical support for other coastal studies using ICESat-2 data.

Keywords: photon-counting lidar; signal photon extraction; coastal zone photon classification; ICESat-2

Citation: Song, Y.; Ma, Y.; Zhou, Z.; Yang, J.; Li, S. Signal Photon Extraction and Classification for ICESat-2 Photon-Counting Lidar in Coastal Areas. *Remote Sens.* **2024**, *16*, 1127. https://doi.org/10.3390/rs16071127

Academic Editor: Jorge Vazquez

Received: 24 January 2024
Revised: 9 March 2024
Accepted: 18 March 2024
Published: 22 March 2024

1. Introduction

As the interaction area between sea and land, coastal zones are areas where the resources and population concentrate. Also, coastal zones have the most frequent human activity and biological reproduction in the world and are the habitats of marine organisms such as coral reefs [1,2]. Coastal topography is the fundamental data for coastal construction [3] and provides important data support for scientific studies of marine biodiversity, global warming, and crustal movement [4]. Many platforms and their borne devices have been developed for coastal topographic measurement, such as airborne laser bathymetry (ALB) [5–7]. The main limitation of these measurement techniques is the spatial coverage, which cannot be conducted at a global scale.

In the past few decades, satellite imagery has achieved large-scale coastal zone monitoring [8,9], and multispectral/hyperspectral imagery has been used to conduct bathymetry in shallow waters [10–13]. However, the imagery mainly has advantages in providing horizontal features, boundaries, and classifications but may lack vertical information. Fortunately, ICESat-2 equipped with the Advanced Topographic Laser Altimeter System (ATLAS) and launched in 2018 can accurately obtain the surface profile and even underwater bottom in shallow waters, which can provide vertical reference data for multispectral imagery [14–16] and have very promising applications in coastal topographic surveys [17–19].

Photon-counting detectors in ICESat-2/ATLAS can respond to received photons and record their arrival time tags, but not the intensity of signal, which significantly differs from conventional lidars with waveform-recording capabilities [20,21]. As a result, an efficient

method is needed to extract the signal photons from the geolocated photons, which contain a large number of noise photons. Up to now, based on the spatial distribution characteristics of lidar points, many methods have been proposed to extract the signal photons or points [22], e.g., the spatial nonlinear clustering algorithms including the Gaussian Mixture Model (GMM), quadtrees, Density-Based Spatial Clustering of Applications with Noise (DBSCAN) [23–25], etc. The three algorithmic models have different clustering methods: the GMM algorithm determines the point cloud category via probability density model estimation, the quadtree achieves the identification of point clouds in different spatial regions via spatial segmentation, and DBSCAN classifies point clouds based on the density of the domain in which the point cloud is located, in which DBSCAN was successfully applied to ICESat-2 geolocated photons [26–29]. All of these methods have been proved to be effective to some degree under the complex geological conditions of coastal areas, e.g., the GMM and quadtree algorithms should further consider the effect of different ground reflectance during signal extraction, while the DBSCAN should consider the difference of photon densities between the land and water interface.

These signal extraction methods focus on detecting signal photons from different surfaces but do not include surface-type classification. The photon classification algorithms for vegetation covered and mountainous inland areas have been well developed and show unique advantages in land classification, e.g., the classification of ground and canopy photons based on the differential, regressive, and Gaussian adaptive nearest neighbor (DRGANN) model [30]; the moving curve fitting algorithm, which fits the surface contours to separate ground photons from canopy photons [31]; the progressive triangular irregular network (TIN) densification, which constructs triangular grids to separate ground photons from canopy photons [32]; and the point-region quadtree-based signal detection algorithm (PRQSD), which converts the spatial distribution of photons into a point-region quadtree [24]. However, the above methods are not fully applicable to coastal areas with more complex terrain at the land–water interface, where the distribution of signal photons is significantly different between land and water. In coastal areas, the classification information about signal photons is also very useful in seafloor topography measurement, tidal flat construction [7,16,33], etc. Currently, signal photon classifications in coast areas occurs with the aid of the auxiliary data [21]. The task of both signal photon extraction and classification in coastal areas is very challenging. The difficulty of achieving individual classification of ICESat-2 data limits the large-scale applications associated with obtaining global bathymetric points.

This study focuses on simultaneously addressing the problems of signal photon extraction and surface type classification in coastal areas that have complex topography with land and water photon mixing. Combined with land photon extraction algorithms and marine photon extraction algorithms, we build adaptive photon extraction and classification algorithms for the land–ocean interface areas in the absence of prior data. Specifically, we compare the proposed algorithm with other algorithms, including the extraction results from ATL08 [30]. The algorithmic accuracy of this study is better than those of single-photon processing algorithms for the land or sea surface detections. In summary, the algorithm proposed in this study lays a good foundation for subsequent study in coastal areas.

2. Materials and Methods

The laser pulse frequency of ICESat-2/ATLAS was 10 kHz, which created an adjacent laser footprint spacing of ~0.7 m at ground surfaces. The ICESat-2 data from the National Snow and Ice Data Center (NSIDC) were divided into three levels. The Level-2 ATL03 product provided the time tag, latitude, longitude, and ellipsoidal height of each geolocated photon and corrected the elevation according to the atmospheric correction and tidal correction models [34]. The ATL03 product also gave the confidence level of each photon, which was used to assist in distinguishing signal photons from noise photons. The geolocated photons from the ATL03 product were the input data in this study. The ATL08 product provided the classification labels for geolocated photons in the ATL03 product. Since it was

mainly applied to vegetated areas, the photons were labeled as noise, ground, canopy, and top of canopy [30]. The classification labels from ATL08 were used for comparison with the results of this study.

To evaluate the method performance, we selected eight coastal zone orbital data values for the experiment, using the approach from Lin et al. to identify the geographic regions [35], mainly considering the global distribution and typical topography of coastal areas. The eight data values contained different latitudes and different coastal zone topographies, i.e., artificial coasts, natural coasts, islands, and reefs. Figure 1 illustrates the geographical distribution of experimental data in the world, and Figure 2 illustrates raw geolocated photons from ATL03 products. The IceSat-2 data from years 2018, 2020, and 2021 were used in this study for 8 regions (Figure 1) for model creation (Table 1).

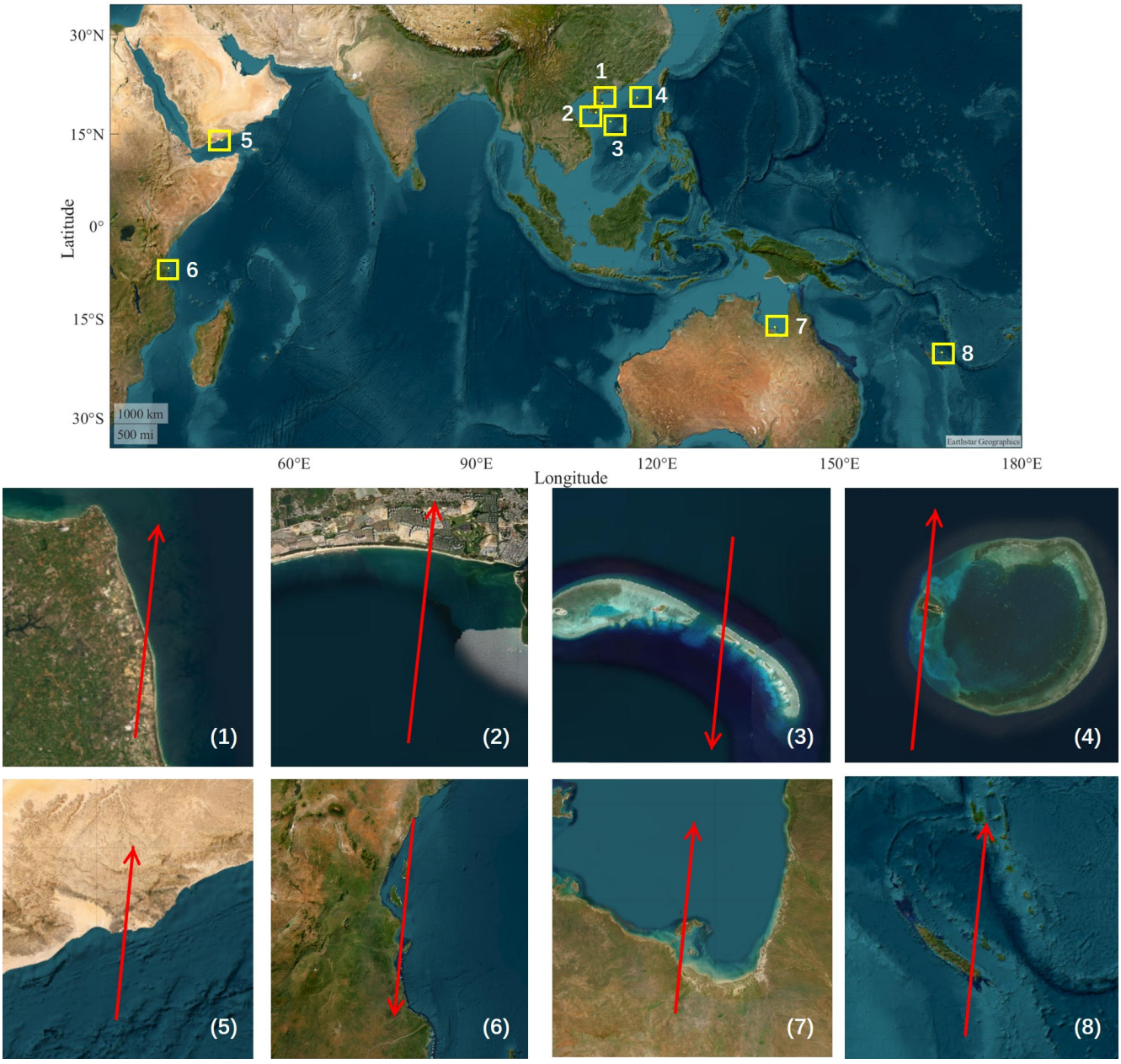

Figure 1. Geographical distribution of experimental data. The direction of the arrow represents the direction of movement of the satellite during transit. Eight ground tracks of ICESat-2 include artificial coasts, natural coasts, islands, and reefs. The file ID from serial numbers (**1**–**8**) in the figure are given in Table 1.

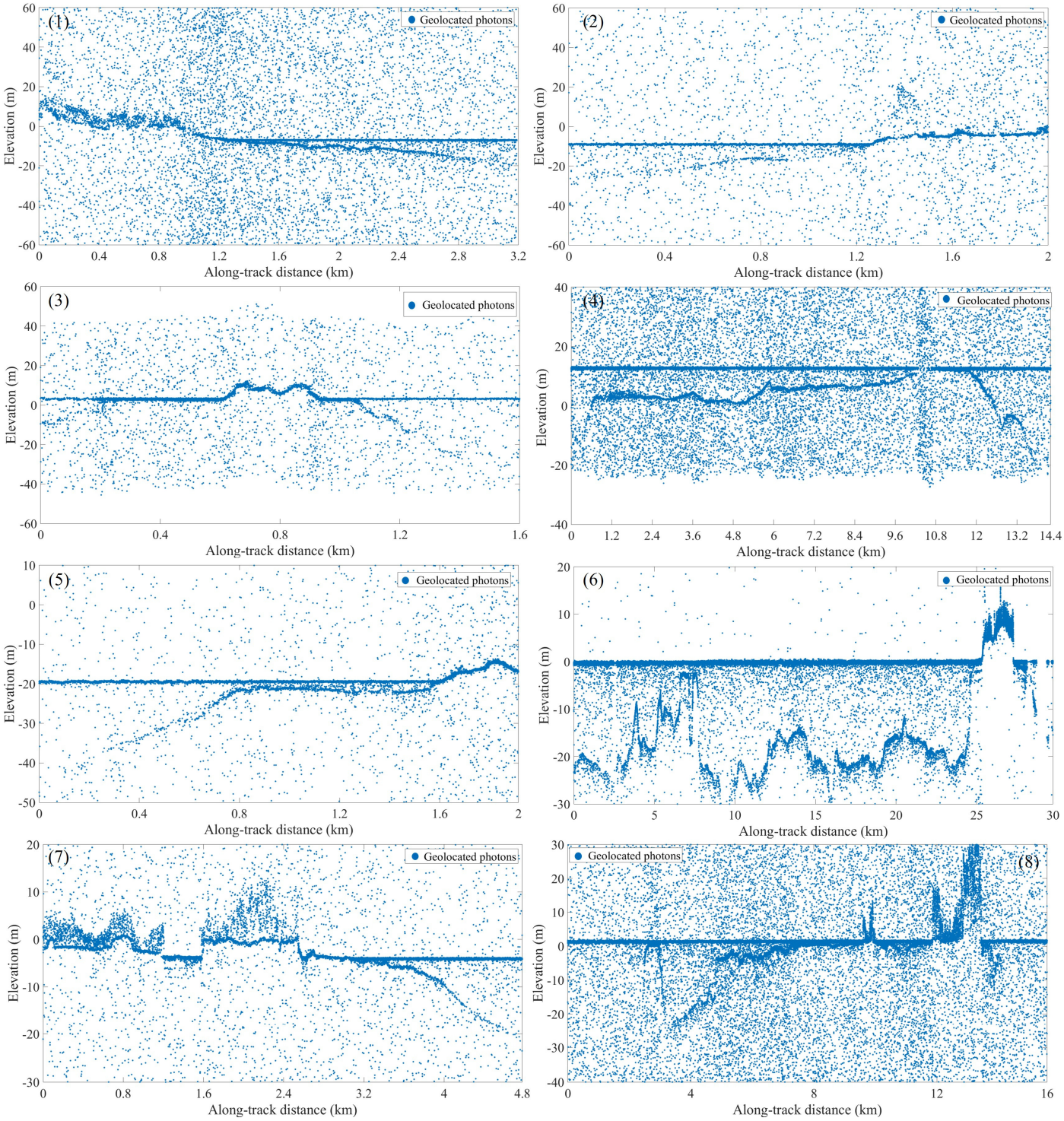

Figure 2. Raw geolocated photons from ATL03 products for tracks **1** to **8**, corresponding to numbers (**1**–**8**) in Figure 1.

This study focused on addressing the extraction and classification of geolocated photons of ICESat-2 in coastal areas, and the flow chart of the proposed method is shown in Figure 3. Specifically, the signal photon extraction module included Step (1) and Step (2), i.e., the rough and precise extraction stages corresponding to the orange and yellow boxes in Figure 3, respectively. In Step (3), based on the initial label of photons after the extraction and the spatial distribution characteristics of photons reflected from different surfaces, the extracted signal photons are divided into four categories: the ground, ground covering,

water surface, and bottom. In Step (4), to further reduce the influence of the water scattering effect on extracting bottom signal photons, we used the inverse distance weighting (IDW) method to determine the continuous along-track bottom profile, providing a basis for subsequent bathymetric correction and application.

Table 1. The ICESat-2 granule file ID used in this study.

1	ATL03_20200620024106_13070701_005_01
2	ATL03_20200727010031_04840801_005_01
3	ATL03_20210214031837_07961007_005_01
4	ATL03_20200322063541_13220601_005_01
5	ATL03_20181015121227_02580101_005_01
6	ATL03_20181018004230_02960108_005_01
7	ATL03_20181018060533_02990114_005_01
8	ATL03_20181031034043_04960114_005_01

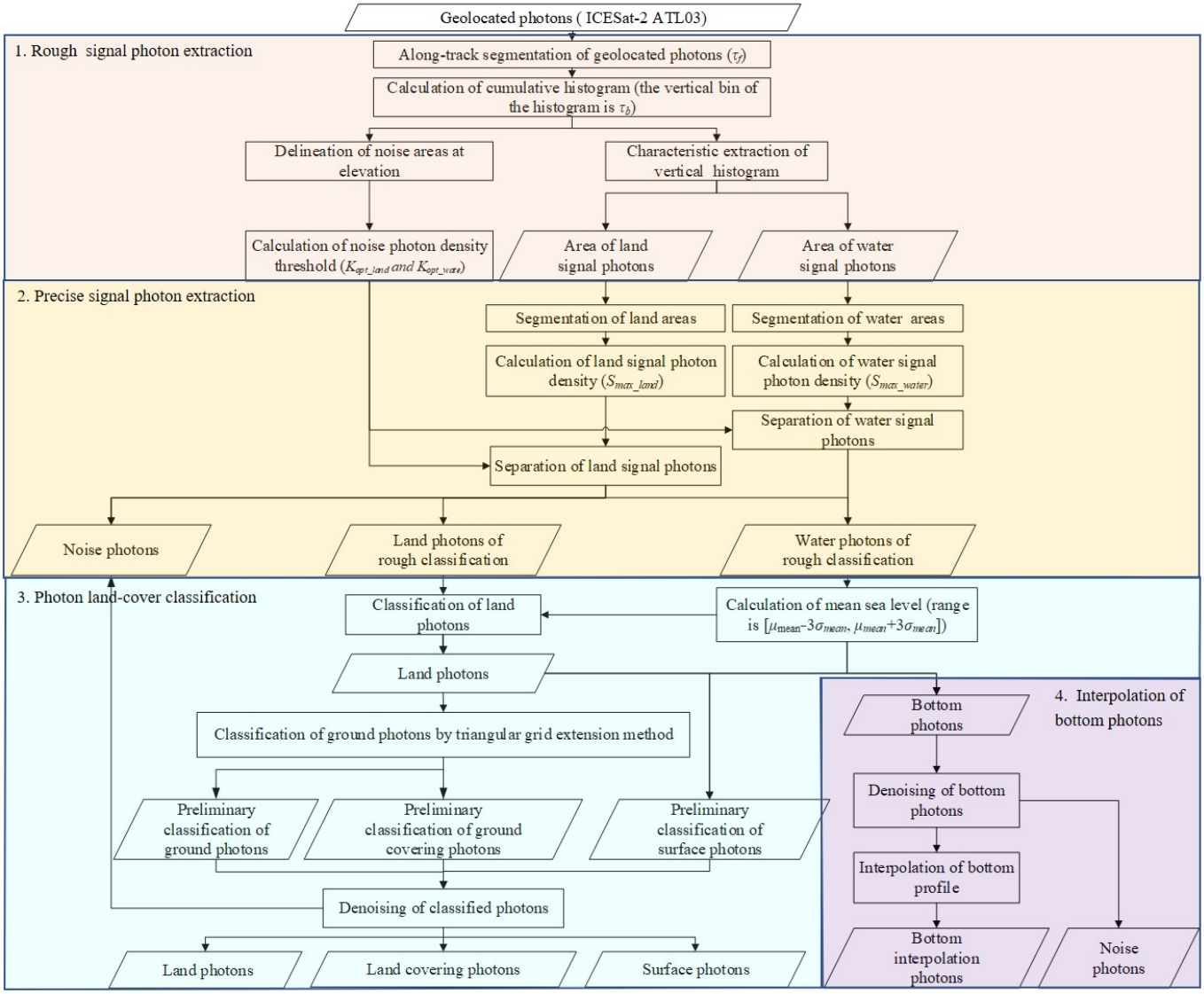

Figure 3. The flow chart of extraction and classification for the geolocated photons of ICESat-2 in coastal areas. The photon processing flow is divided into four main blocks: rough signal photon extraction, precise signal photon extraction, photon land-cover classification, and the interpolation of bottom photons.

2.1. Signal Photon Extraction in Coastal Areas

The target characteristics of different objects (especially the surface characteristics, such as the reflectance, roughness, slope, etc.) resulted in different spatial distributions of signal photons, whereas noise photons (mainly from solar background) generally filled in the entire space within the range gate of ICESat-2 and satisfied uniform distribution [36]. As a result, object-oriented signal extraction was essential. With the help of the national land cover database (NLCD), the along-track surface types were obtained from satellite optical images with a 30-meter spatial resolution [37]. However, some problems existed when using the satellite imagery, e.g., the water and land boundary varied due to the tide effect, and the acquisition time of ICESat-2 was probably different to that of satellite imagery. A simple, effective, and fast method that did not require ancillary data was essential for the preliminary preprocessing when utilizing ICESat-2 data for bathymetric measurements. Based on the histogram of geolocated photons within different spatial sizes, each photon was assigned an initial feature label (signal on water/land or noise) in the rough extraction. Then, based on the direction of the maximum photon density distribution on water surfaces/lands, the size of the search range and the threshold of signal photon density were determined, which enabled the separation of signal photons from noise in the precise extraction.

2.1.1. Rough Signal Photon Extraction

The rough extraction process was used to preliminarily divide geolocated photons into noise and signal, as well as preliminarily determine the along-track boundary between land and water. This process was designed to quickly determine the possible spatial area containing signal photons (especially reducing the height range from hundreds of meters to tens of meters in the ATL03 product) and sharply decrease the amount of data storage. The rough extraction process was as follows.

(a) The geolocated photons from the ATL03 product were segmented (with a segment length of τ_f = 100 m) according to the relative along-track distance, e.g., four typical segments were selected, and they are illustrated in Figure 4a. We noted that the relative along-track distance of each photon could be calculated from its corresponding longitude and latitude or its time tag, multiplying the flight speed of ICESat-2.

(b) The cumulative histogram in elevation was generated using the photons within each segment, and the vertical bin of the histogram was τ_b = 1 m to ensure that the influence of vegetation fluctuation on the peaks of the histograms was minimized and that the water surface and bottom elevations could be effectively distinguished, e.g., four histograms are shown in Figure 4b–e, which correspond to the four along-track segments in Figure 4a.

(c) Preliminary water photons and land photons were distinguished according to the distribution characteristics of the vertical histogram in each segment. Specifically, the peaks of the histogram were extracted. The maximum peak P_{max}, i.e., the maximum photon number in all vertical bins, was detected. The equivalent Lambert reflectance of sea surfaces was ~0.15–0.20, with a moderate wind speed and nearly nadir incidence, which was generally close to the reflectance of the bare land and vegetation. As a result, near the interface, the amplitudes of the land, water, and possible bottom generally had the same orders of magnitude. To remove noise features and preserve the main features in each 100-meter length segment, other peaks (with a number of N_p) whose photon numbers were greater than one-third times of P_{max} were detected. When the number of detected peaks (N_p + 1) within the segment was less than or equal to 2, such as in Figure 4c–e, the segment was preliminarily considered to be the water area; otherwise, the current segments were considered to be land, such as in Figure 4b. We noted that areas of flat sandy beach near the interface of land and water may have been misclassified as water. This misclassification did not affect the subsequent photon extraction, and the possibly misclassified photons were corrected in signal-photon classification.

(d) In each classified water or land segment, the elevation of the maximum peak was determined to be the reference elevation H_{ref}. Normally, H_{ref_land} is larger than H_{ref_water}. In

each segment, the reference elevation H_{ref} was used as the vertical center of signal photons to determine the vertical range where signal photons were possibly located. Specifically, the photons whose elevation was beyond the vertical range in $[H_{ref} - H_{down}, H_{ref} + H_{up}]$ were identified as noise and discarded to decrease the total photon number. Waves introduced vertical fluctuations on water surfaces. The elevations of signal photons on water surfaces were generally centered at the local mean sea level and distributed with the RMS (root mean square) wave height. In water segments, the downward buffer H_{down} had to at least cover the maximum bathymetry depth of ICESat-2 (generally 30 m). The upward buffer H_{up} had to cover the possible wave heights, and generally, 10 m was sufficient. Compared with water surfaces such as in Figure 4e, the elevations of photons in land areas such as in Figure 4b had a larger upward buffer (especially considering the coverings). In land segments, the downward and upward buffers were set to 30 m, considering the topographic fluctuation and the covering (such as vegetation and buildings) [33].

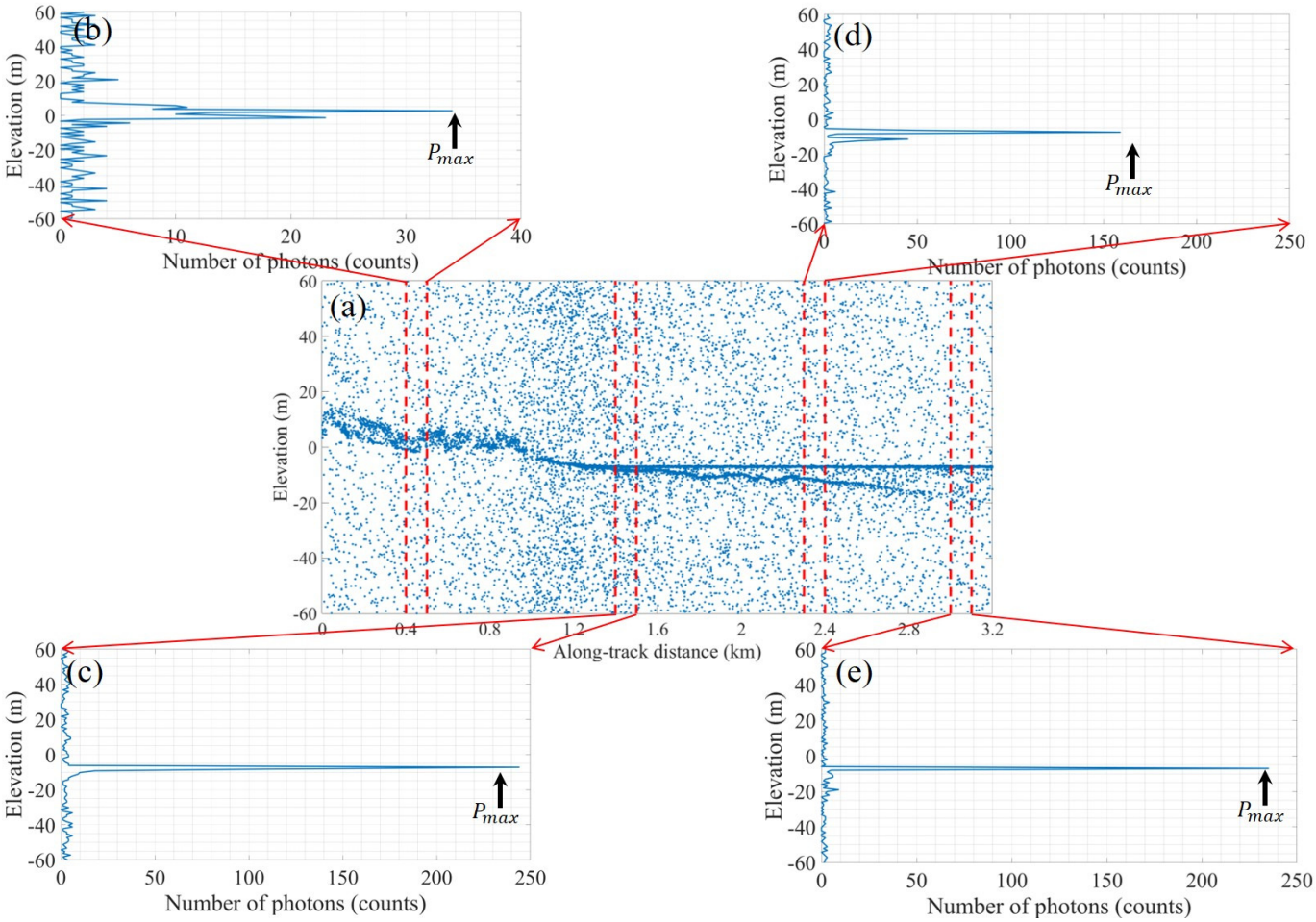

Figure 4. (**a**) Sampled ATL03 geolocated photons and elevation histograms of each along-track segment in coastal areas; (**b**) elevation histogram of a land segment; (**c**) elevation histogram near the land–sea interface; (**d**) elevation histogram of a water segment with bottom photons; (**e**) elevation histogram of a water segment without bottom photons. The used data correspond to the ground track shown in Figure 1(1), which had a relatively high noise level during the daytime.

In addition, the photons within the vertical range $[H_{ref} + H_{up}, H_{ref} + H_{up} + H_{noise}]$ that was above the possible signal photon vertical range were used to estimate noise photon densities in preparation for precise signal photon extraction. H_{noise} is the noise buffer, which was set to 10 m during the daytime and increased to 30 m at night due to the number of background noise photons dramatically decreasing. The result of the rough

extraction (using the data in Figure 4) is shown in Figure 5, which illustrates the preliminary classification of land and water areas in the along-track direction and signal/noise vertical range in elevation for each segment.

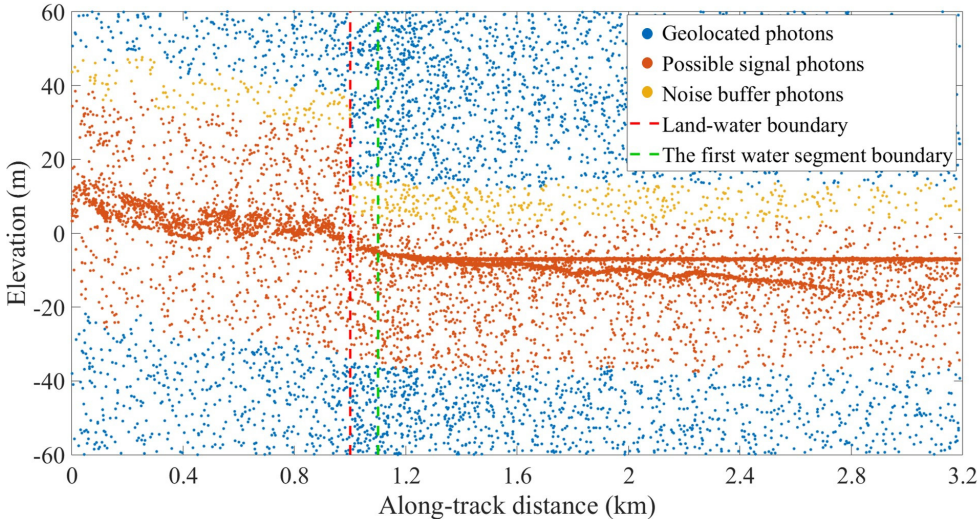

Figure 5. Sampled ATL03 geolocated photons and rough extraction result. The vertical red dashed line represents the preliminary land–water boundary in the along-track distance, and the area between the red dashed line and the green dashed line is the first water segment along the track, which is filtered out in calculating the mean sea level to reduce the effect of lapping waves.

2.1.2. Precise Signal Photon Extraction

Firstly, the noise photon density (i.e., the photon number per squared meters) was calculated in each segment (using yellow photons in Figure 5). For land and water areas, the average noise photon density of N_{noise} (including N_{noise_land} and N_{noise_water}) and the standard deviation of σ_{noise} (including σ_{noise_land} and σ_{noise_water}) were separately calculated using all land or water segments. Although we could calculate the expected noise number under a set of given environmental parameters, the number of actual photons satisfied a Poisson distribution within a neighborhood. In other words, the number of actual photons randomly varied within a neighborhood. Hence, the photon density threshold between noise and signal was set to $K_{opt} = N_{noise} + 3\sigma_{noise}$, which theoretically removed 99% of noise photons.

Then, for each photon within the possible signal vertical range (i.e., red photons in Figure 5), the neighboring photon density within an ellipse with a semi-long axis of r_a and semi-short axis of r_b was calculated. Specifically, the center of the ellipse was located at current photon $p(x_p, y_p)$, where x_p is the along-track distance and y_p is the elevation. For the photon $p(x_p, y_p)$, its neighboring photon $q(x_q, y_q)$ was within the ellipse when satisfying

$$dist(p,q) = \sqrt{\frac{(x_p - x_q)^2}{r_a^2} + \frac{(y_p - y_q)^2}{r_b^2}} \leq 1 \quad (1)$$

After searching for all photons within the ellipse, the photon number density S_0 for the photon $p(x_p, y_p)$ could be calculated as the photon number within the ellipse divided by the ellipse area $\pi r_a r_b$.

Considering the possible slope of the land and bottom, additional rotations of the searching ellipse with respect to x-axis (i.e., the along-track distance) were implemented.

For coastal areas, we used the rotation angles θ ranging from $-20°$ to $20°$ at an interval of $5°$. For the searching ellipse with rotation, Equation (1) had to be modified as follows:

$$dist(p,q) = \sqrt{\frac{\Delta x^2}{r_a^2} + \frac{\Delta y^2}{r_b^2}} \leq 1 \tag{2}$$

where Δx and Δy satisfy

$$\begin{aligned} \Delta x &= \cos\theta \cdot (x_p - x_q) + sin\theta \cdot (y_p - y_q) \\ \Delta y &= \sin\theta \cdot (x_p - x_q) - \cos\theta \cdot (y_p - y_q) \end{aligned} \tag{3}$$

For each photon, the photon number densities with different rotations were calculated, respectively, i.e., S_0, S_5, S_{10}, S_{15}, S_{20}, S_{-5}, S_{-10}, S_{-15}, S_{-20}, in which the maximum photon number density was used as the density S_{max} for the current photon. A photon within the possible signal vertical range (i.e., red photons in Figure 5) was identified as a signal photon when S_{max} was larger than the threshold K_{opt}, i.e., $S_{max} \geq K_{opt}$. We noted that the threshold of land K_{opt_land} was different from (generally larger than) that of waters K_{opt_water} due to the higher reflectance of lands.

After the precise extraction of signal photons, Figure 6 illustrates the extracted signal photons from the red photons first depicted in Figure 5, where a sampled searching ellipse with the maximum photon number density is also shown using the blue ellipses in Figure 6b. For different study areas, the effectiveness of the signal photon extraction could be improved by adjusting (r_a, r_b).

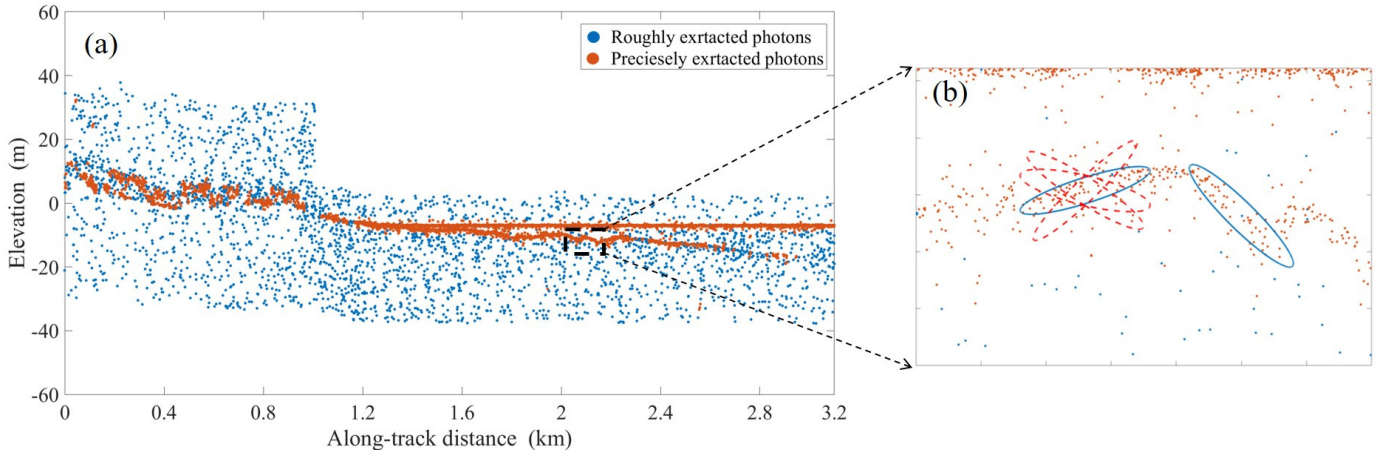

Figure 6. (**a**) Sampled results of precise signal photon extraction. The input data are the results of rough signal photon extraction first depicted in Figure 5. The signal search ellipse has a long axis r_a of 20 m and a short axis r_b of 1 m. (**b**) Enlarged area in (**a**), which illustrates the searching ellipses with different rotations and the maximum photon number density using the blue ellipses.

2.2. Signal Photon Classification and Bottom Profile Interpolation

In this section, the extracted signal photons will be classified into four categories in coastal areas: the ground, ground covering, water surface, and bottom. To reduce the water scattering effect on the bottom photons, the along-track bottom profile will be interpolated via the inverse distance weighting method.

2.2.1. Signal Photon Classification

To classify the photons for water segments, the local mean sea level was calculated first. The reference elevation H_{ref_water} within each water segment, which was obtained by the histogram peak, as shown in Figure 4c–e, was used as the i-th average sea surface height μ_{h_i}. For the i-th water segment, the standard deviation σ_{h_i} of elevations of signal photons within the current segment was calculated. We noted that the first water segment near the

land–water boundary, e.g., the segment between the red dotted line and the green dotted line in Figure 5, is not involved in avoiding the influence of lapping waves on the mean sea level. The $\mu_{\text{h\_i}}$ and σ_{h_i} in all segments were averaged to calculate the mean sea level μ_{mean} and mean standard deviation σ_{mean} that is generally related to the wave height, respectively. Then, the signal photons whose heights were within $[\mu_{\text{mean}} - 3\sigma_{mean}, \mu_{mean} + 3\sigma_{mean}]$ were marked as sea surface photons. The signal photons with heights of less than $\mu_{mean} - 3\sigma_{mean}$ were classified as bottom photons, whereas the signal photons with heights greater than $\mu_{mean} + 3\sigma_{mean}$ were marked as noise photons.

In the classification of land segments, it was necessary to divide land photons into ground photons and ground covering photons. An improved classification of triangular grid was used to conduct the land photon classification in coastal areas as follows [38,39]:

(1) Framing potential ground photons. As the land topography was more complex and variable than that of water surfaces, each land segment was reduced to sub-segments with a length τ_c of 10 m. In mountain areas, the elevations of ground photons were typically located at 0–15% of the elevation range of all land signal photons [40]. In this study, the land photon whose elevation was within 0–15% of the signal elevation range in each sub-segment was considered to be a potential ground photon.

(2) Determining initial ground photons. The photon density S_{max} for each photon was calculated in the precise signal photon extraction subsection of Section 2.1.2. In each sub-segment, the average photon density S_{mean} was calculated using the photon densities of all potential ground photons within the current sub-segment. The potential ground photons with a density greater than S_{mean} were marked as the initial ground photons. The potential ground photon whose elevation was less than the initial ground photons was marked as a noise photon, and other remaining potential ground photons were processed in the next step.

(3) Determining ground photons [39]. All remaining potential ground photons were processed via the triangular grid extension method. Specifically, within each sub-segment, two initial ground photons that had the shortest Euclidean distances to each remaining potential ground photon were selected to construct a triangle, and the potential ground photon was used as the top. Potential ground photons are categorized as follows: (a) The height D and two angles A_1 and A_2 were calculated in each triangle, which is shown in Figure 7. (b) When the parameters A_1, A_2, and D were less than the thresholds (A_1 and A_2 were set to 45° and D was 0.5 m), the current potential ground photon is marked as an initial ground photon. (c) The remaining potential ground photons repeated the Steps (a) and (b) until no new initial ground photons were generated, and then all initial ground photons were classified as ground photons.

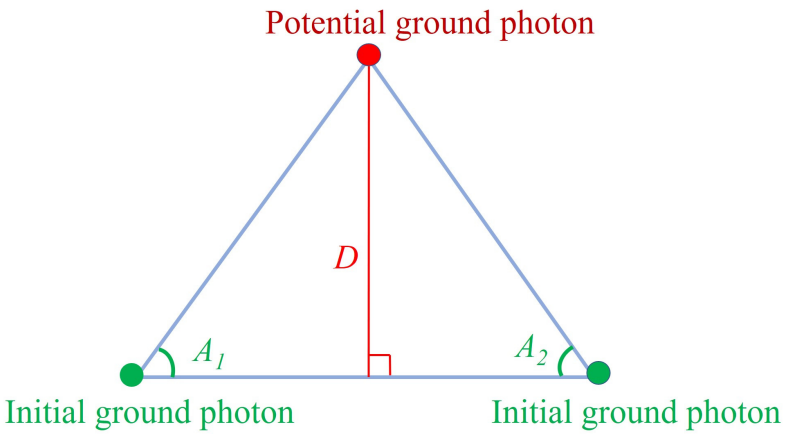

Figure 7. Two initial ground photons that have the shortest Euclidean distances to each potential ground photon are selected to construct a triangle, and the potential ground photon is used as the top.

After determining the ground photons, the remaining signal photons were classified as ground covering photons in land segments. To further remove possible noise, the classified ground, ground covering, and water surface signal photons were filtered using the DBSCAN algorithm [37,40]. Figure 8 illustrates the final signal photons with their corresponding classification labels.

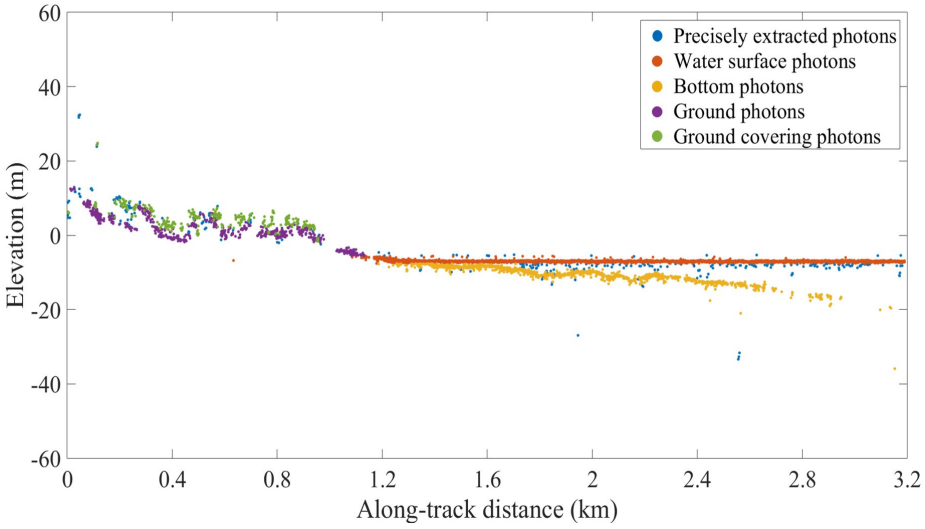

Figure 8. Final signal photons with their corresponding classifications, where the blue photons are filtered out as noise compared to the red points in Figure 6.

2.2.2. Generating Seafloor Profile from Bottom Photons

The input data in this section are the signal photons with bottom classification labels. Firstly, in each segment, the mean height H_b and standard deviation σ_b of bottom photons were calculated to further remove possible noise, and the photons that were beyond the range of $[H_b - 3\sigma_b, H_b + 3\sigma_b]$ were considered to be noise. Then, the inverse distance weighting method was used to interpolate the bottom profile. Specifically, the along-track coordinates of the bottom profile were uniformly arranged with an along-track interval of τ_{b_c}. When the number of bottom photons was greater than 50 counts per 100 m in the along-track distance, τ_{b_c} was set to 10. When less than 50 counts, τ_{b_c} was 20 m. However, when less than 25 counts, the underwater profile could not be determined via interpolation. For each profile point, five bottom photons that have the shortest Euclidean distances were selected, in which the weight of the i-th bottom photon could be expressed as follows:

$$w_i = \frac{l_i^{-2}}{\sum_{j=1}^{n} l_j^{-2}} \tag{4}$$

l_i represents the distance between the i-th bottom photon and current profile point in the along-track direction, and n represents the number of selected bottom photons (n = 5 in this study). The elevation of current profile point $h_{profile}$ can be expressed as follows:

$$h_{proflie} = \sum_{i=1}^{n} w_i h_{bottom\_i} \tag{5}$$

where h_{bottom_i} is the elevation of the i-th selected bottom photon. Figure 9 illustrates the calculated bottom profile.

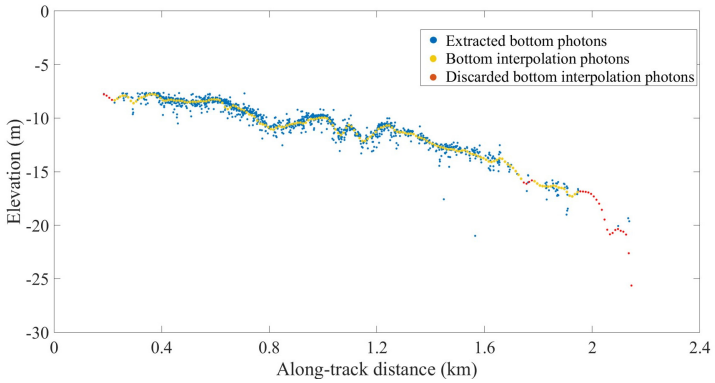

Figure 9. Bottom profile generated by the bottom photons and via the inverse distance weighting (IDW) method. The blue points are the extracted bottom photons, the yellow points are bottom interpolation photons, and the red points are discarded bottom interpolation photons.

Due to the rare number of local underwater photon point clouds, local over-interpolation can occur when using the IDW interpolation algorithm. Therefore, we optimized the algorithm for this problem: The underwater photons were relatively sparse. The interpolation interval τ_{b_c} was 10 m to ensure that there would be at least one underwater photon near each interpolation point. Seafloor contour interpolation points with fewer than 5 underwater photons per 50 m in the along-track distance were removed to prevent over-interpolation (red points in Figure 9 are discarded bottom interpolation points).

Remarkably, the bottom interpolated photons shown in Figure 9 needed to be error corrected in order to find the real bottom topography photons. ICESat-2 bathymetry includes signal photon extraction, bathymetry correction, and popular research that is currently being performed to realize the bathymetry of satellite-borne remotely sensed imagery using laser point clouds as control points, and Ma et al. have performed a pretty full set of that research [14]. Chen et al. performed signal extraction, water depth error correction, and comparison with observed data [41]. The original intention of this study was to conduct preliminary signal extraction and classification of the geolocated photons in complex coastal areas, which provide basic data for the subsequent research into the surface or underwater. In other words, the main purpose of this study was signal classification and signal extraction, which is labeling each signal photon for classification. Further bathymetric corrections were further investigated by subsequent authors for their own purposes.

2.3. Accuracy Verification Metrics

To quantitatively verify the accuracy of the proposed method, the manual signal extraction results were used as true signal labels. *TP* represents the true signal photons that are correctly extracted, *FP* represents the noise photons that are misclassified as signal photons, *FN* represents the true signal photons that fail to be extracted, and *TN* represents the number of correctly classified noise photons. The recall ratio can be expressed as follows:

$$P_{ec} = \frac{TP}{TP + FN} \tag{6}$$

and the precision ratio can be expressed as follows:

$$P_{re} = \frac{TP}{TP + FP} \tag{7}$$

The harmonic mean of the recall ratio and precision ratio F was used to quantitatively evaluate the extraction effectiveness, where

$$F = \frac{2P_{re}P_{ec}}{P_{re} + P_{ec}} \tag{8}$$

3. Results

This study focuses on the extraction and classification of signal photons in coastal areas. To explore the applicability of the proposed method, Figure 10 illustrates the rough extraction results of the four typical geomorphological features of coastal areas (four tracks of the eight-track data were selected to represent typical coastal area topography, and the extraction and classification precision of the eight-track data are shown in Tables 2 and 3), which correspond to the artificial coasts, natural coasts, islands, and reefs in Figure 1, serial numbers 1 to 4, respectively. The results indicate that the rough extraction can divide ATL03 geolocated photons into signal and noise areas and assign initial labels to photons without using external prior data. The results in Figure 10 demonstrate the performance of dividing geolocated photons into land and water segments based on histogram characteristics in Figure 4 and the performance of separating possible signal photon regions from noise regions. Figure 10 sharply discards the noise photons and selects the noise buffer photons (the yellow points), which are used to estimate the noise level in each segment and calculate the signal density threshold. In addition, Figure 10 provides the preliminary land–water boundary in the along-track distance (the red vertical lines).

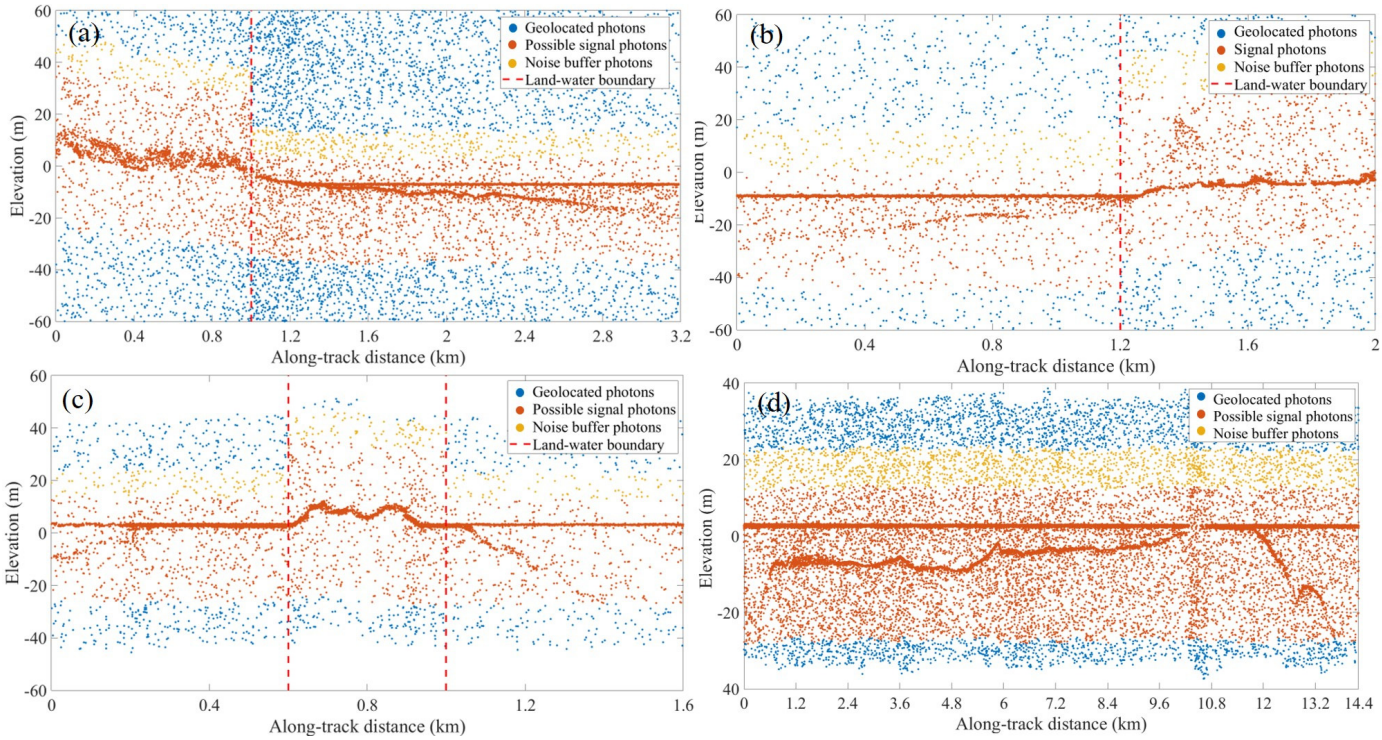

Figure 10. Results of the rough extraction in different coastal areas: (**a**) Artificial coasts; (**b**) natural coasts; (**c**) islands; (**d**) reefs. Determining the possible signal photon regions based on the peak location of the elevation histograms in each segment (see Figure 4). Blue points are ATL03 geolocated photons and yellow points are marked as noise buffer and used to estimate the noise level in each segment, which is further used to calculate the signal density threshold. The vertical red dashed line represents the preliminary land–water boundary in the along-track distance. The data in (**a**–**d**) correspond to the tracks in the subsets of (1) to (4) in Figure 1, respectively.

Then, using the input data in Figure 10, Figure 11 illustrates the results of precisely extracted and classified photons. The proposed method generally performs well in signal photon extraction and classification in different coastal area topographies. However, in the enlarged part in Figure 11c, when the elevations of the seafloor are very close to that of the sea surface (<1 m), some bottom photons and a few water backscattered photons are misclassified as sea surface photons. The reason for this is that the water surface has a certain elevation range due to waves and the water scattering effect is relatively strong in

the subsurface. In this case, manual intervention or segmentation is generally needed to correct these misclassified photons. Before interpolating the underwater profile, Figure 11c is manually corrected for misclassified bottom photons to obtain Figure 12c.

Table 2. Performance metrics (*F*) of the signal photon extraction results.

Data Number	Method in This Paper (%)	DBSCAN (%)	HDBSCAN (%)	GMM (Gaussian Mixture Model) (%)	QC (Quadtree Classification) (%)	ATL08 (%)
1	88.2	83.7	84.3	86.8	61.9	84.7
2	83.3	82.4	80.5	72.8	67.9	72.8
3	93.9	82.6	90.3	92.1	63.9	42.1
4	91.2	80.7	88.5	84.8	84.3	89.0
5	86.4	73.4	85.5	86.0	63.7	85.6
6	87.3	82.7	87.2	84.3	87.0	84.5
7	90.2	87.5	87.7	83.2	78.5	85.3
8	89.1	78.0	87.2	85.8	90.4	83.5

Table 3. Performance metrics of surface type classification results.

Data Number	Classified Types	Quantities of Types	P_{ec} (%)	P_{re} (%)	*F* (%)	*Kappa* (%)
1	Water surface	5578	93.4	82.3	87.5	86.3
	Bottom	1237	91.9	83.1	87.2	
	Ground	781	93.6	97.4	95.5	
	Ground covering	334	93.4	82.3	87.5	
2	Water surface	29,440	98.0	85.2	91.2	81.3
	Bottom	222	93.4	77.5	84.7	
	Ground	3456	89.1	82.1	85.5	
	Ground covering	1073	95.1	75.4	84.1	
3	Water surface	3772	96.8	75.6	84.9	77.8
	Bottom	1322	51.7	80.9	63.1	
	Ground	753	91.4	87.9	89.6	
	Ground covering	119	81.2	90.8	85.7	
4	Water surface	145,633	91.2	98.9	94.9	85.9
	Bottom	3264	80.7	87.8	84.1	
5	Water surface	5706	97.5	97.4	97.5	86.6
	Bottom	1232	92.2	86.7	89.4	
	Ground	1752	90.0	91.4	90.2	
	Ground covering	59	70.4	71.2	70.8	
6	Water surface	83,805	96.8	95.6	96.3	85.1
	Bottom	4468	69.7	87.1	77.0	
	Ground	3222	92.8	96.6	94.7	
	Ground covering	606	69.7	86.1	77.0	
7	Water surface	10,742	95.0	98.8	96.9	83.7
	Bottom	989	82.7	78.5	80.5	
	Ground	3801	94.5	93.3	93.9	
	Ground covering	697	60.3	86.2	71.0	
8	Water surface	37,437	94.5	96.5	95.5	75.9
	Bottom	10876	88.4	82.6	85.4	
	Ground	853	60.2	71.3	65.3	
	Ground covering	909	64.4	81.4	71.9	

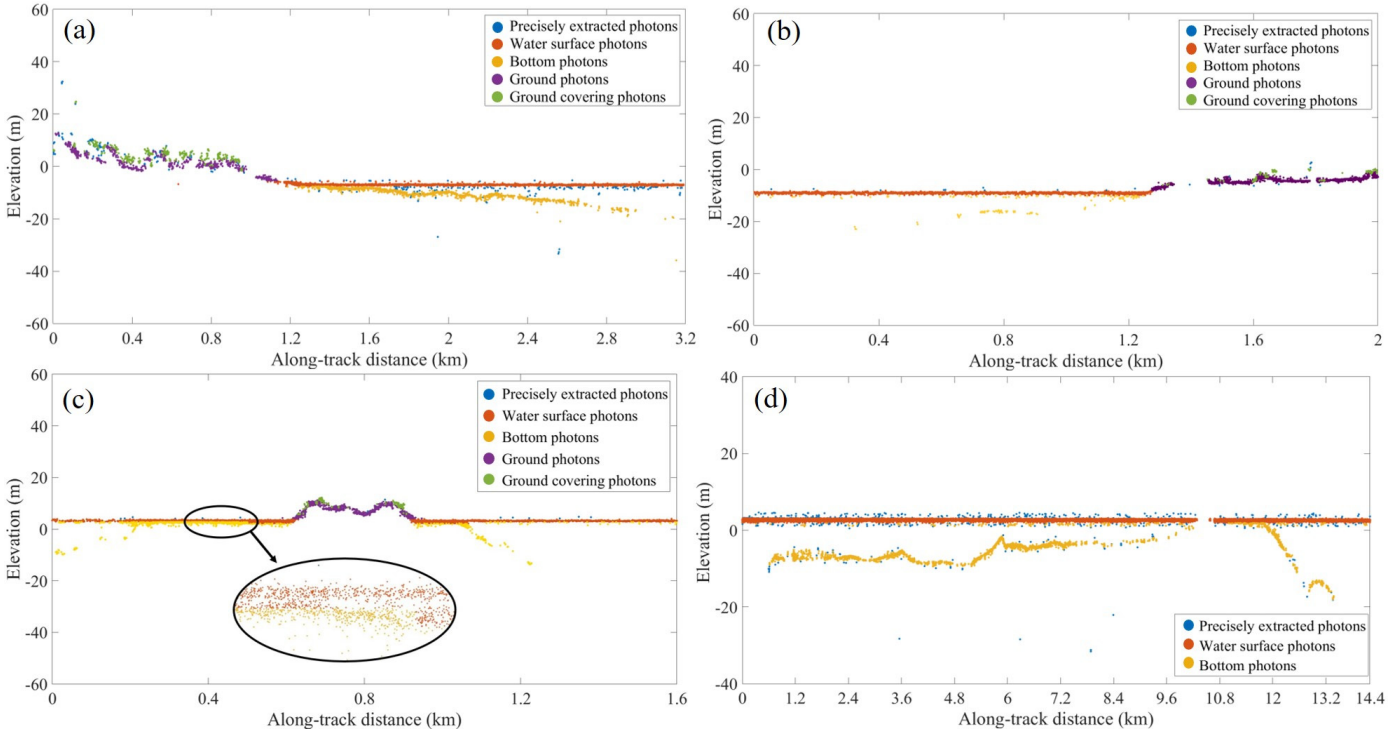

Figure 11. Precise extraction and classification results of photons in different coastal areas: (**a**) artificial coasts; (**b**) natural coasts; (**c**) islands; (**d**) reefs. The input data are from Figure 10.

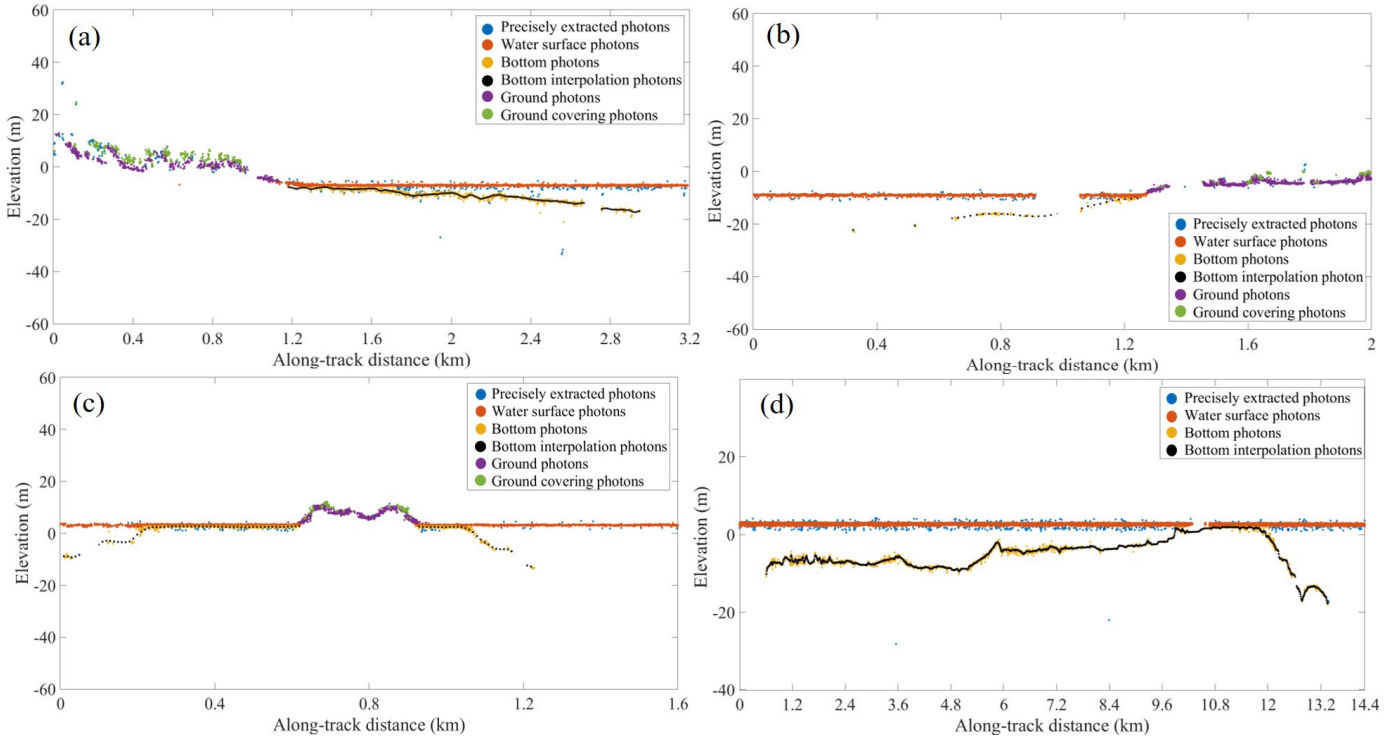

Figure 12. Final results of our method with interpolated seafloor profiles (black points): (**a**) artificial coasts; (**b**) natural coasts; (**c**) islands; (**d**) reefs. The input data are from Figure 11. (**a**) has a low density of bottom photons (between 25 and 50 photons per 100 m in the along-track distance), and, thus, the interpolation interval of τ_{b_c} is set to 20 m. The along-track interpolation interval of τ_{b_c} for (**b**–**d**) is set to 10 m.

In Figure 11, the bottom photons have less density than the surface and ground photons, and Figure 11 illustrates the interpolated seafloor profiles (black points) via the IDW method, which successfully draws successive bottom profiles and reduces the effect of water column scattering on the bottom photons. In addition, a successive bottom profile is of great importance for the water depth correction and extraction.

The DBSCAN [29], HDBSCAN [25], Gaussian Mixture Model (GMM) [23], quadtree classification (QC) [24], and ATL08 algorithms [30] were used as a comparison experiment for the proposed method. The signal photon extraction accuracy *F* values of the six methods are shown in Table 2, and the signal extraction performances of different methods are shown in Figure 13. The proposed method performs better than other methods, and its signal photon extraction accuracy *F* values were better than 0.9 in all eight test regions, which reflects the better robustness of the method in this paper for the processing of complex topographic data in coastal areas.

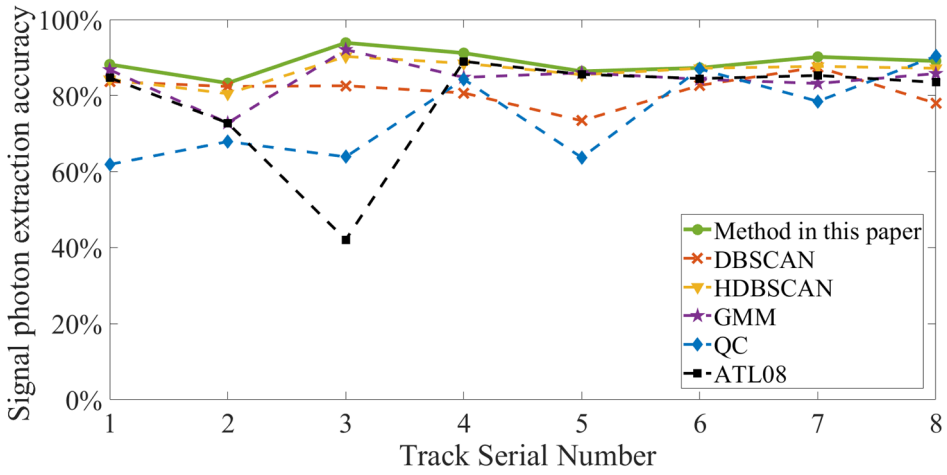

Figure 13. Signal extraction accuracy F values of different methods, where the horizontal coordinates 1–8 correspond to the ICESat-2 track numbers 1–8 in Figure 1.

However, the DBSCAN, HDBSCAN, Gaussian Mixture Model (GMM), and quadtree classification (QC) methods only focus on detecting signal photons from different surfaces and do not include the surface type classification. The ATL08 product contains classification labels for signaling photons [30]; thus, the comparison of the classification results of this study with the ATL08 classification results is illustrated in Figures 14 and 15.

In the ATL08 product, the signal photons are classified into three categories (i.e., the ground, canopy, and top canopy). Coastal areas normally have complex topographies, meaning that the ATL08 algorithm is not suitable for detecting signal photons there, as illustrated in Figure 14(1b,3b) and Figure 15(6b,7b), which misclassify water surface and bottom photons as the top canopy and ground photons, respectively. In addition, many underwater photons are misclassified as noise photons. Meanwhile, as the ground and water surfaces are not distinguished in Figures 14 and 15, the water and land boundaries are not well detected in the ATL08 product. As a result, the algorithm proposed in this study focuses on the land–water interface areas to extract and classify signal photons without relying on prior data, which will lay a good foundation for the subsequent study of coastal areas.

For the regions of ground-track numbers 1 and 5 in Figure 1, two more periods of geolocated photons are selected to illustrate the classification results. In Figure 16, the proposed method still has a good classification performance for the same coastal areas using data from different periods, which doubly verify its strong applicability in coastal areas. Please note that since different tracks of ICESat-2 do not spatially overlap with each other, the geolocated photons from different periods are quite different.

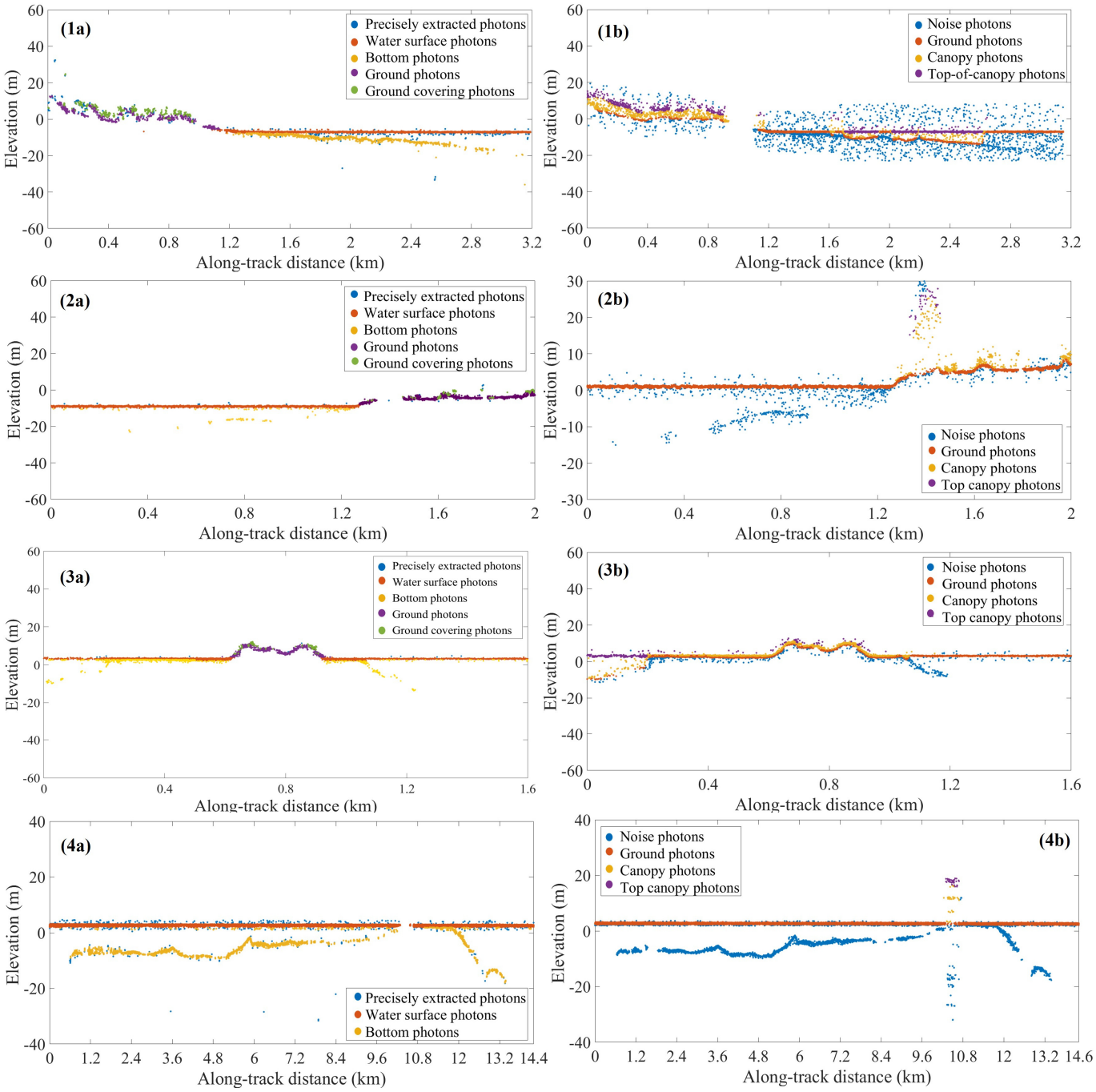

Figure 14. Comparison between the classification results of the proposed algorithm and ATL08 algorithm. The serial numbers (**1a**–**4a**) are the classification results of our algorithm, and the serial numbers (**1b**–**4b**) are the ATL08 classification results.

For surface type classification, the Kappa coefficient is used in addition to P_{ec}, P_{re}, and F [39]. The true classification labels are obtained via the high-resolution images and manual identification. In Table 3, the classification results of surface types are presented. The artificial coast has the highest classification accuracy, as the terrain is flatter and the covering vegetation is relatively sparse, meaning that the method is more likely to identify the feature photons. The island has the worst performance, and combined with Figure 11c (which corresponds to data number 4 in Table 3), the recall ratio of the bottom photons (P_{ec} = 0.517) and the precision ratio of the surface photons (P_{re} = 0.756) are mainly influenced by the mixing of bottom and surface photons in very shallow waters. The

proposed method also shows good results in photon classification, with an average Kappa of ~0.83. Thus, the proposed method achieves two tasks in coastal areas, i.e., signal photon extraction and classification, and has a good robustness.

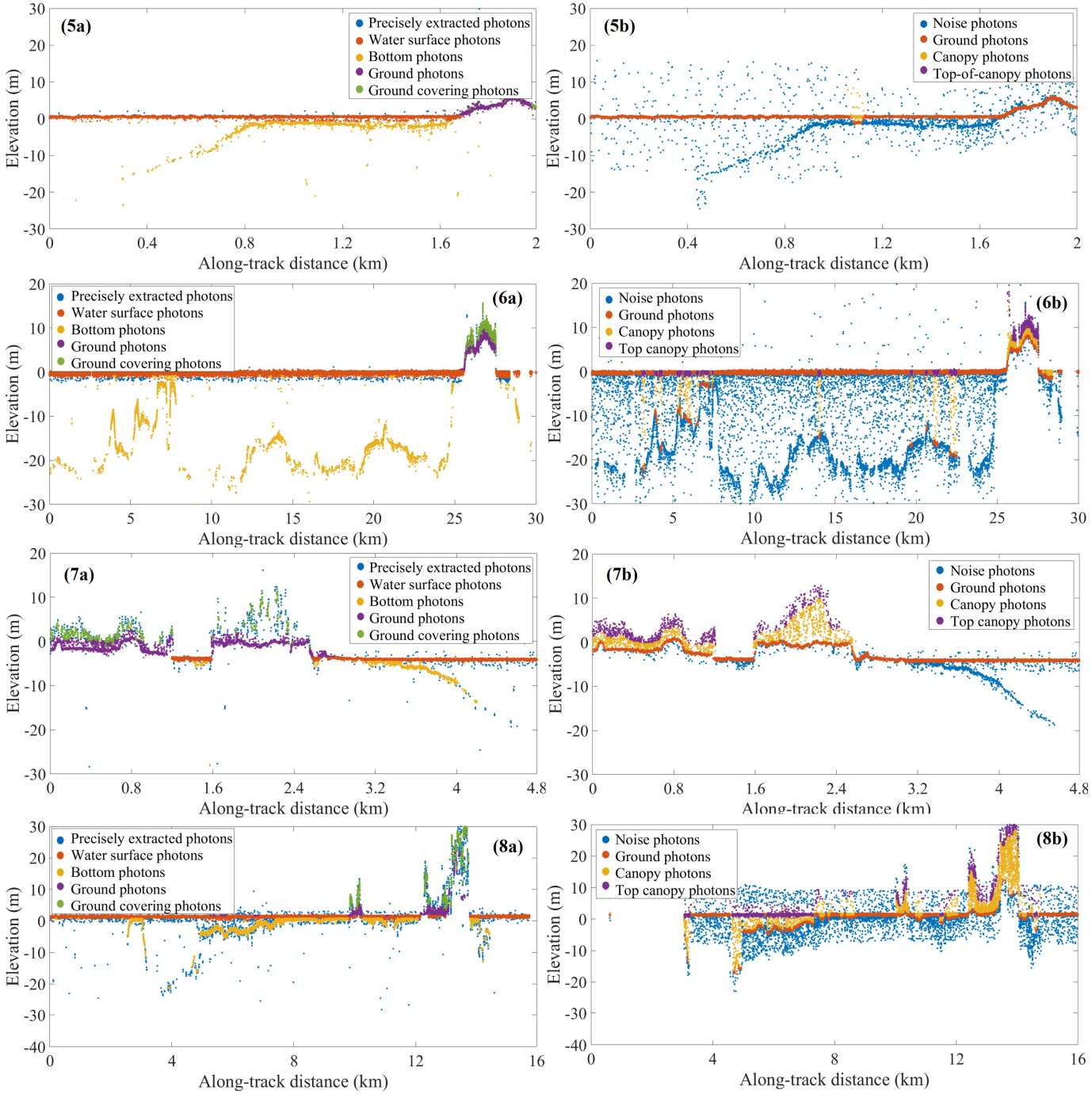

Figure 15. Comparison between the classification results of the proposed algorithm and ATL08 algorithm. The serial numbers (**5a**–**8a**) are the classification results of our algorithm, and the serial numbers (**5b**–**8b**) are the ATL08 classification results.

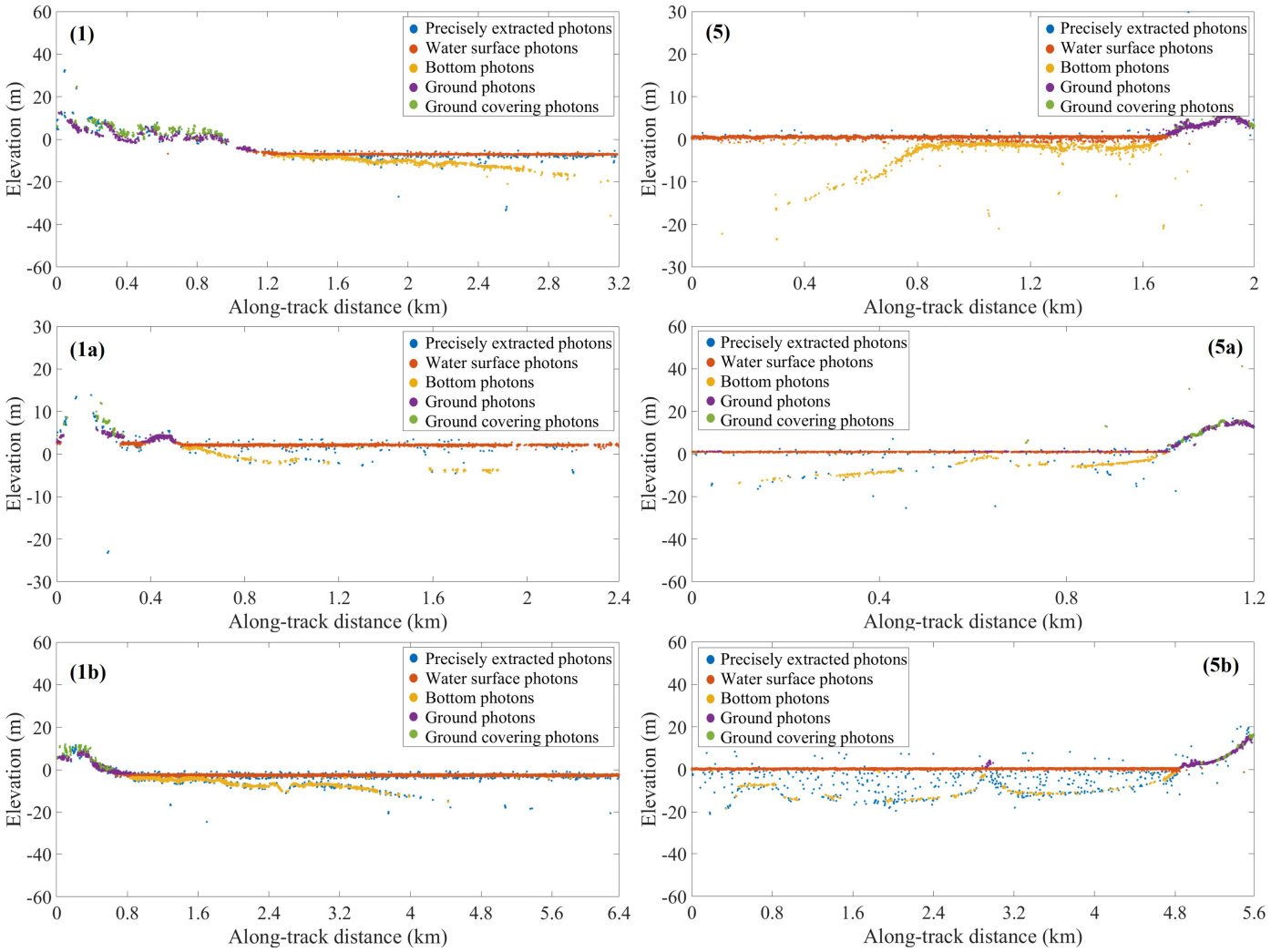

Figure 16. Classification results of ICESat-2 geolocated photons obtained at different times in the same experimental areas. The data of the track numbers 1 and 5 in Figure 1 are selected for the comparison of classification results at multiple times, i.e., (**1**) and (**5**) correspond to the classification results of track number (1) and track number (5) in Figure 1, respectively. (**1a**), captured on 17 September 2021, and (**1b**), captured on 23 July 2022, are within same study area as (**1**), captured on 20 June 2020, whereas (**5a**), captured on 14 January 2019, and (**5b**), captured on 12 January 2020, are within same study area as (**5**), captured on 15 October 2018.

4. Discussion

4.1. Selection of Empirical Thresholds

The empirical thresholds used in this study are explained in this section:

(1) The along-track segment length of geolocated photons τ_f is 100 m. Due to the complex terrain at the land–water interface, we set τ_f as 100 m, which is identical to the segment length used in the ATL08 processing algorithm. Within one segment, only one type of topography (i.e., sea surface or land) is allowed to improve the processing efficiency.

(2) The vertical interval t_b of 1 m for cumulative histograms. As the topography slope near coastal zones is relatively small, a small vertical interval t_b ensures that the influence of vegetation fluctuation on the histogram peaks is minimized, and then the water surface and bottom peaks can be effectively distinguished.

(3) The signal photon intervals H_{up} and H_{down} in water segments. In water segments, the downward buffer H_{down} should at least cover the maximum bathymetric depth of ICESat-2 (generally 30 m). The upward buffer H_{up} should cover the possible wave heights, and 10 m is generally sufficient. According to the level definition of sea states, nine wave

levels are classified [42]. Level 7 has a significant wave height (4σ) ranging from 6 to 9 m, and fishing boats should be docked in harbors during their occurrence, which rarely happens except for in strong storm circumstances. In practice, the sea states above Level 7 are not suitable for activities such as offshore measurements.

(4) The signal photon intervals H_{up} and H_{down} in land segments. In land segments, the downward and upward buffers are set to 30 m, considering the topographic fluctuation and its covering, with an assumption of vegetation and a building height less than 30 m from the shoreline.

(5) The signal photon searching ellipse with a semi-long axis of r_a, semi-short axis of r_b, and range of rotation angle from -20° to 20°. The distribution density of signal photons in the along-track direction is greater than that in the vertical direction. During the daytime, the signal searching ellipses are searched with a semi-long axis r_a of 5 m and semi-short axis r_b of 0.5 m to ensure that the photon density is calculated with seven to eight laser shots in each searching ellipse. At night, benefitting from the weak background, the searching range is extended to 10 m on the long half-axis to ensure that the searching ellipse contains signal photons from 14 to 15 laser shots. In terms of coastal topography around the globe, most shallow underwater terrains have slopes of less than 20°, and, thus, the range of rotation angles is basically covered [43]. In addition, as the direction of ICESat-2 ground tracks has an azimuth angle with the slope direction, the along-track slope is less than the surface and bottom slope. If the rotation angle is further increased, it would be helpful to extract signal photons for extreme cases, such as cliffs, but it would consume more time during the signal extraction.

4.2. Advantages and Limitations of This Algorithm

The method proposed in this study achieves land–sea classification without the assistance of prior data. In Li et al.'s study, the random forest classifier is modeled and trained to classify the land cover types [44], which achieves more surface type classifications but needs the training data set. The method is still based on density clustering and aims to improve the performance of DBSCAN. A typical drawback of DBSCAN is the difficulty in selecting the best discrimination parameters, which leads to a poor performance using the same parameters where the noise level dramatically varies. In practice, our previous studies have proved that the noise levels of water areas significantly differ from those of land areas [45,46]. To consider this issue, in this study, the noise photon density in different regions is used as a reference for the threshold setting, taking into account the variability in land and sea reflectivity rather than setting a fixed threshold. From above Table 2, the proposed algorithm has better performance metrics (F) more suitable for coastal areas compared with the currently used HDBSCAN, Gaussian Mixture Model (GMM), quadtree, and ATL08 algorithms.

The proposed method also has good results in photon classification, with an average Kappa of ~0.83 (as shown in Table 3 of the manuscript). However, the classification accuracy is relatively low for data numbers 3 and 8, which correspond to islands surrounding by very shallow waters. This method, including signal photon extraction and classification, is not always effective for categorizing surface and bottom photons in very shallow waters. Due to the ocean waves and backscattered photons from subsurface, the surface and bottom photons are easily confused in very shallow waters, i.e., as illustrated within black ellipse in Figure 11c. In this case, this method finds it difficult to separate the surface photons from the bottom photons based on the surface photon elevation distribution, and the two types of photons need to be separated via manual intervention. Even in this case, it might just be theoretically indistinguishable when the surface and bottom photons are completely intermixed in the spatial region. This challenging issue will be the focus of future studies.

5. Conclusions

We propose a method from signal photon extraction to feature classification for ICESat-2 geolocated photon data in coastal areas. The method achieves the separation of signal

and noise photons without the support of external data. Based on the elevation of water surface photons as a reference and the triangular grid for land segments, the extracted signal photons are further divided into four categories: water surface, bottom, ground, and ground covering. Finally, the bottom photons are interpolated to obtain continuous underwater profiles. The proposed method is tested using the ATL03 datasets from four typical terrains.

The results indicate that the proposed method has a better performance than the single-data processing method in coastal areas, where the surface types are more complex. Generally, the extraction accuracy of signal photons reaches over 0.90, most of the classification accuracy indicators *F* exceed 0.80, and the Kappa coefficients of the four typical surface types in coastal areas exceed 0.75, achieving high consistency in classification. However, some limitations exist, e.g., in very shallow waters, the current method is unable to precisely separate the water surface and bottom photons as their distances are very close, as shown in Figure 11c. In addition, the proposed method can be considered for application to inland water and inland wetland topography for signal photon extraction and classification.

Author Contributions: Conceptualization, S.L. and Y.M.; methodology, Y.S.; validation, Y.S., J.Y. and Y.M.; writing—original draft preparation, Y.S.; writing—review and editing, Y.S. and S.L.; visualization, Z.Z. and J.Y.; supervision, Y.M.; funding acquisition, Y.M. All authors have read and agreed to the published version of the manuscript.

Funding: This research was funded in part by the National Natural Science Foundation of China, under Grant 42371440, and in part by the Hubei Provincial Key Research and Development Program, China, under Grant 2022BID6.

Data Availability Statement: Data can be obtained from the authors through a reasonable request.

Acknowledgments: The authors sincerely thank the NASA National Snow and Ice Data Center (NSIDC) for distributing the ICESat-2 ATL03 data (https://doi.org/10.5067/ATLAS/ATL03.005 (accessed on 13 October 2022)) and Esri for providing the imagery that was used in this article.

Conflicts of Interest: The authors declare no conflicts of interest.

References

1. Nicholls, R.J.; Cazenave, R. Sea-level rise and its impact on coastal zones. *Science* **2010**, *328*, 1517–1520. [CrossRef]
2. Murray, N.J.; Phinn, S.R.; Dewitt, M.; Ferrari, R.; Fuller, R.A. The global distribution and trajectory of tidal flats. *Nature* **2019**, *565*, 222–225. [CrossRef]
3. Jin, H.; Huang, C.; Lang, M.W.; Yeo, I.-Y.; Stehman, S.V. Monitoring of wetland inundation dynamics in the delmarva peninsula using landsat time-series imagery from 1985 to 2011. *Remote Sens. Environ.* **2017**, *190*, 26–41. [CrossRef]
4. Gonalves, G.R.; Santos, S.; Duarte, D.; Santos, J.G. Monitoring Local Shoreline Changes by Integrating UASs, Airborne LiDAR, Historical Images and Orthophotos. In Proceedings of the 5th International Conference on Geographical Information Systems Theory, Applications and Management GISTAM, Crete, Greece, 3–5 May 2019; pp. 126–134. [CrossRef]
5. Wong, H.C.; Antoniou, A. Two-dimensional signal processing techniques for airborne laser bathymetry. *IEEE Trans. Geosci. Remote Sens.* **1996**, *34*, 57–66. [CrossRef]
6. Zhao, X.; Zhao, J.; Zhang, H.; Zhou, F. Remote sensing of suspended sediment concentrations based on the waveform decomposition of airborne lidar bathymetry. *Remote Sens.* **2018**, *10*, 247. [CrossRef]
7. Xu, W.; Guo, K.; Liu, Y.; Tian, Z.; Tang, Q.; Dong, Z.; Li, J. Refraction error correction of Airborne LiDAR Bathymetry data considering sea surface waves. *Int. J. Appl. Earth Obs. Geoinf.* **2021**, *102*, 102402. [CrossRef]
8. Dimitris, P.; Dimosthenis, T.; Peter, R.; Nektarios, C. On the use of Sentinel-2 for coastal habitat mapping and satellite-derived bathymetry estimation using downscaled coastal aerosol band—ScienceDirect. *Int. J. Appl. Earth Obs. Geoinf.* **2019**, *80*, 58–70. [CrossRef]
9. Bishop-Taylor, R.; Nanson, R.; Sagar, S.; Lymburner, L. Mapping Australia's dynamic coastline at mean sea level using three decades of Landsat imagery. *Remote Sens. Environ.* **2021**, *267*, 112734–112753. [CrossRef]
10. Lyzenga, D.R. Passive remote sensing techniques for mapping water depth and bottom features. *Appl. Opt.* **1978**, *17*, 379–383. [CrossRef]
11. Lee, Z.; Carder, K.L.; Mobley, C.D.; Steward, R.G.; Patch, J.S. Hyperspectral remote sensing for shallow waters. I. A semianalytical model. *Appl. Opt.* **1998**, *37*, 6329–6338. [CrossRef]

12. Mobley, C.D.; Sundman, L.K.; Davis, C.O.; Bowles, J.H.; Downes, T.V.; Leathers, R.A.; Montes, M.J.; Bissett, W.P.; Kohler, D.D.; Reid, R.P. Interpretation of hyperspectral remote-sensing imagery by spectrum matching and look-up tables. *Appl. Opt.* **2005**, *44*, 3576–3592. [CrossRef]
13. Kutser, T.; Hedley, J.; Giardino, C.; Roelfsema, C.; Brando, V.E. Remote sensing of shallow waters—A 50 year retrospective and future directions. *Remote Sens. Environ.* **2020**, *240*, 111619. [CrossRef]
14. Ma, Y.; Xu, N.; Liu, Z.; Yang, B.; Li, S. Satellite-derived bathymetry using the ICESat-2 lidar and Sentinel-2 imagery datasets. *Remote Sens. Environ.* **2020**, *250*, 112047. [CrossRef]
15. Babbel, B.J.; Parrish, C.E.; Magruder, L.A. ICESat-2 elevation retrievals in support of satellite-derived bathymetry for global science applications. *Geophys. Res. Lett.* **2021**, *48*, e2020GL090629. [CrossRef] [PubMed]
16. Nguyen, V.-A.; Ren, H.; Huang, C.-Y.; Tseng, K.-H. Bathymetry derivation in shallow water of the South China Sea with ICESat-2 and Sentinel-2 data. *J. Appl. Remote Sens.* **2021**, *15*, 044513. [CrossRef]
17. Hermosilla, T.; Wulder, M.A.; White, J.C.; Coops, N. Land cover classification in an era of big and open data: Optimizing localized implementation and training data selection to improve mapping outcomes. *Remote Sens. Environ.* **2022**, *268*, 112780–112796. [CrossRef]
18. Jain, A.; Ramakrishnan, R.; Thomaskutty, A.; Agrawal, R.; Rajawat, A.; Solanki, H. Topography and morphodynamic study of intertidal mudflats along the eastern coast of the Gulf of Khambhat, India using remote sensing techniques. *Remote Sens. Appl. Soc. Environ.* **2022**, *27*, 100798. [CrossRef]
19. Zhang, X.; Chen, Y.; Le, Y.; Zhang, D.; Yan, Q.; Dong, Y.; Han, W.; Wang, L. Nearshore bathymetry based on ICESat-2 and multispectral images: Comparison between sentinel-2, landsat-8, and testing Gaofen-2. *IEEE J. Sel. Top. Appl. Earth Obs. Remote Sens.* **2022**, *15*, 2449–2462. [CrossRef]
20. Parrish, C.E.; Magruder, L.A.; Neuenschwander, A.L.; Forfinski-Sarkozi, N.; Jasinski, M. Validation of icesat-2 atlas bathymetry and analysis of atlas's bathymetric mapping performance. *Remote Sens.* **2019**, *11*, 1634. [CrossRef]
21. Xie, H.; Xu, Q.; Ye, D.; Jia, J.; Sun, Y.; Huang, P.; Li, M.; Liu, S.; Xie, F.; Hao, X. A comparison and review of surface detection methods using MBL, MABEL, and ICESat-2 photon-counting laser altimetry data. *IEEE J. Sel. Top. Appl. Earth Obs. Remote Sens.* **2021**, *14*, 7604–7623. [CrossRef]
22. Zhang, J.; Kerekes, J. An adaptive density-based model for extracting surface returns from photon-counting laser altimeter data. *IEEE Geosci. Remote Sens. Lett.* **2014**, *12*, 726–730. [CrossRef]
23. Ma, Y.; Jin, Q.; Mei, X.; Dai, X.; Fan, F.; Li, H.; Huang, J. Hyperspectral unmixing with Gaussian mixture model and low-rank representation. *Remote Sens.* **2019**, *11*, 911. [CrossRef]
24. Xie, H.; Sun, Y.; Xu, Q.; Li, B.; Guo, Y.; Liu, X.; Huang, P.; Tong, X. Converting along-track photons into a point-region quadtree to assist with ICESat-2-based canopy cover and ground photon detection. *Int. J. Appl. Earth Obs. Geoinf.* **2022**, *112*, 102872. [CrossRef]
25. Rehman, K.; Fareed, N.; Chu, H.-J. NASA ICESat-2: Space-Borne LiDAR for Geological Education and Field Mapping of Aeolian Sand Dune Environments. *Remote Sens.* **2023**, *15*, 2882. [CrossRef]
26. He, L.; Pang, Y.; Zhang, Z.; Liang, X.; Chen, B. ICESat-2 data classification and estimation of terrain height and canopy height. *Int. J. Appl. Earth Obs. Geoinf.* **2023**, *118*, 103233. [CrossRef]
27. Lao, J.; Wang, C.; Nie, S.; Xi, X.; Long, H.; Feng, B.; Wang, Z. A new denoising method for photon-counting LiDAR data with different surface types and observation conditions. *Int. J. Digit. Earth* **2023**, *16*, 1551–1567. [CrossRef]
28. Zheng, X.; Hou, C.; Huang, M.; Ma, D.; Li, M.J.I.G.; Letters, R.S. A Density and Distance-Based Method for ICESat-2 Photon-Counting Data Denoising. *IEEE Geosci. Remote Sens. Lett.* **2023**, *20*, 6500405. [CrossRef]
29. Zhong, J.; Liu, X.; Shen, X.; Jiang, L. A Robust Algorithm for Photon Denoising and Bathymetric Estimation Based on ICESat-2 Data. *Remote Sens.* **2023**, *15*, 2051. [CrossRef]
30. Neuenschwander, A.L.; Pitts, K.L.; Jelley, B.P.; Robbins, J.; Klotz, B.; Popescu, S.C.; Nelson, R.F.; Harding, D.; Pederson, D.; Sheridan, R. *ATLAS/ICESat-2 L3A Land and Vegetation Height, Version 5*; National Snow and Ice Data Center Distributed Active Archive Center: Boulder, CO, USA, 2021. [CrossRef]
31. Moussavi, M.S.; Abdalati, W.; Scambos, T.; Neuenschwander, A. Applicability of an automatic surface detection approach to micro-pulse photon-counting lidar altimetry data: Implications for canopy height retrieval from future ICESat-2 data. *Int. J. Remote Sens.* **2014**, *35*, 5263–5279. [CrossRef]
32. Nie, S.; Wang, C.; Xi, X.; Luo, S.; Li, G.; Tian, J.; Wang, H. Estimating the vegetation canopy height using micro-pulse photon-counting LiDAR data. *Opt. Express* **2018**, *26*, A520–A540. [CrossRef]
33. Liu, C.; Li, J.; Tang, Q.; Qi, J.; Zhou, X. Classifying the nunivak island coastline using the random forest integration of the sentinel-2 and icesat-2 data. *Land* **2022**, *11*, 240. [CrossRef]
34. Neumann, T.A.; Brenner, A.; Hancock, D.; Robbins, J.; Saba, J.; Harbeck, K.; Gibbons, A.; Lee, J.; Luthcke, S.B.; Rebold, T. *ATLAS/ICESat-2 L2A Global Geolocated Photon Data, Version 4*; National Snow and Ice Data Center Distributed Active Archive Center: Boulder, CO, USA, 2020. [CrossRef]
35. Lin, Y.; Knudby, A.J. Global automated extraction of bathymetric photons from ICESat-2 data based on a PointNet++ model. *Int. J. Appl. Earth Obs. Geoinf.* **2023**, *124*, 103512. [CrossRef]
36. Degnan, J.J. Photon-counting multikilohertz microlaser altimeters for airborne and spaceborne topographic measurements. *J. Geodyn.* **2002**, *34*, 503–549. [CrossRef]

37. Ma, Y.; Zhang, W.; Sun, J.; Li, G.; Xu, N. Photon-counting lidar: An adaptive signal detection method for different land cover types in coastal areas. *Remote Sens.* **2019**, *11*, 471. [CrossRef]
38. Tucker, G.E.; Lancaster, S.T.; Gasparini, N.M.; Bras, R.L.; Rybarczyk, S.M. An object-oriented framework for distributed hydrologic and geomorphic modeling using triangulated irregular networks. *Comput. Geoences* **2001**, *27*, 959–973. [CrossRef]
39. Ivanov, V.Y.; Vivoni, E.R.; Bras, R.L.; Entekhabi, D. Catchment hydrologic response with a fully distributed triangulated irregular network model. *Water Resour. Res.* **2004**, *40*, W11102. [CrossRef]
40. Xie, H.; Ye, D.; Xu, Q.; Sun, Y.; Huang, P.; Tong, X.; Guo, Y.; Liu, X.; Liu, S. A density-based adaptive ground and canopy detecting method for ICESat-2 photon-counting data. *IEEE Trans. Geosci. Remote Sens.* **2022**, *60*, 1–13. [CrossRef]
41. Chen, Y.; Le, Y.; Zhang, D.; Wang, Y.; Qiu, Z.; Wang, L. A photon-counting LiDAR bathymetric method based on adaptive variable ellipse filtering. *Remote Sens. Environ.* **2021**, *256*, 112326. [CrossRef]
42. *GJB4000-2000*; General Specifications for Naval Ships. General Armament Department Military Standard Publishing Department: Beijing, China, 2000.
43. Athanasiou, P.; Dongeren, A.v.; Giardino, A.; Vousdoukas, M.; Gaytan-Aguilar, S.; Ranasinghe, R. Global distribution of nearshore slopes with implications for coastal retreat. *Earth Syst. Sci. Data* **2019**, *11*, 1515–1529. [CrossRef]
44. Binbin, L.; Huan, X.; Xiaohua, T.; Dan, Y.; Kaipeng, S.; Ming, L. Land cover classification using ICESat-2 data with random forest. *Infrared Laser Eng.* **2020**, *49*, 20200292–20200297. [CrossRef]
45. Zhang, Z.; Ma, Y.; Xu, N.; Li, S.; Sun, J.; Wang, X.H. Theoretical background noise rate over water surface for a photon-counting lidar and its application in land and sea cover classification. *Opt. Express* **2019**, *27*, A1490–A1505. [CrossRef] [PubMed]
46. Yang, J.; Zheng, H.; Ma, Y.; Zhao, P.; Zhou, H.; Li, S.; Wang, X.H. Background noise model of spaceborne photon-counting lidars over oceans and aerosol optical depth retrieval from ICESat-2 noise data. *Remote Sens. Environ.* **2023**, *299*, 113858. [CrossRef]